Effect of interface localization on elastic scattering in AlSb/InAs superlattice infrared detectors

M. J. Shaw, M. R. Kitchin, and M. Jaros*
Department of Physics, The University of Newcastle upon Tyne, Newcastle upon Tyne, NE1 7RU, United Kingdom
(Received 8 November 2000; published 23 March 2001)

We employ a microscopic model of AlSb/InAs superlattices to study their dynamical characteristics and the effect of interface bond type. The localization of valence band-edge states at InSb-like interfaces is observed, and we use the elastic scattering cross-section of substitutional defects to probe the superlattice bandstructures. The variation of the scattering properties provides an unambiguous signature of the localized interface states that exist in our model.

DOI: 10.1103/PhysRevB.63.155303 PACS number(s): 73.21.−b, 72.10.Fk

I. INTRODUCTION

The AlSb/InAs heterostructures have been investigated for many years due to their potential for application in optoelectronic and ultra-fast switching devices.[1–9] The combination of large conduction band offset with high electron mobilities make these materials ideally suited to such applications. A feature of these structures that has been the subject of considerable attention is the possibility for two different interface bond types to be formed.[10,11] Due to the lack of a common ion, two different types of interface bond may be formed, AlAs-like or InSb-like. Previous studies[12–15] have shown that the InSb-like interfaces can result in a localization of charge in the valence band-edge state—the so-called ''Tamm state'' initially proposed by Kroemer *et al.*[16] While earlier studies of ours have demonstrated the existence of such localized states using *ab initio* pseudopotential calculations,[12,13] an explicit signature of their presence was not identified. The changes to band-gap energies that we predicted were in agreement with the localization model and available experimental results.[17] However, the existence of such energy shifts could be explained in many ways, and cannot be taken as firm evidence for the presence of localized interface states. In order to understand the microscopic interface properties and their role in device performance, we need to obtain theoretical predictions of the macroscopic effects of interface bond type. What we require are predictions of specific features that relate to the interfaces beyond the simple energy shifts so far predicted, and whose origin can be unambiguously linked to the interface localization.

In this paper, we apply our recently developed strained empirical pseudopotential scheme to study the scattering properties of holes at the valence band edge. The relationship between the interface types and the scattering rates associated with specific defects provides us with a link between the microscopic interface stoichiometry and observable device properties. We demonstrate that the differences between the scattering behaviors of the various interface configurations can act as a signature of the localized interface states.

II. STRAINED EMPIRICAL PSEUDOPOTENTIAL CALCULATIONS

The extension of the conventional empirical pseudopotential scheme to encompass strained systems is described in full elsewhere in the literature.[18,19] Essentially, the method that we apply allows for the full reduction in symmetry associated with strain in the bulk constituents to be accounted for in the superlattice states. In addition, in contrast to the widely used $\mathbf{k}\cdot\mathbf{p}$ methods, the empirical pseudopotentials allow for the correct microscopic description of the structure on an atomistic scale, i.e., it is possible to directly specify the interface type according to the atoms which terminate the various layers in the structure. However, it should be noted that since the empirical pseudopotentials used are fitted with regard to (strained) bulk data, and are sensitive to their local environment, one does not expect that the potentials, which describe the bulk-like superlattice layers (several atoms wide), will necessarily provide a good description of the single interface bond layers. In order that the physics of the interface bonds is included in the potentials used, an additional fitting step is introduced to replicate the localizations and energy shifts that were obtained by our earlier local density *ab initio* calculations.[13]

In this paper, we shall consider three AlSb/InAs superlattice structures of the type studied experimentally by Spitzer *et al.*,[17] all nominally described as 3AlSb/3InAs (where 3AlSb refers to three lattice constants of AlSb), but with different interface configurations: (a) two InSb-like interfaces, (b) two AlAs-like interfaces, and (c) one of each interface. The structures are shown schematically in Fig. 1, both as an atomistic picture showing the individual constituents of each layer and a diagram of the valence band lineup in the various layers. Here we have included a step at the interface layers, as suggested by the argument of Kroemer *et al.*[16]—such a particle-in-a-box band picture has been shown in our earlier studies to provide a useful qualitative insight into the behavior of these structures.[12,13] For each structure the charge density was calculated at the zone-center for the valence band-edge state. The computed charge densities are shown in Fig. 2, and clearly show the localization of charge at the InSb-like interfaces, as seen in Refs. 12 and 13.

From this microscopic model of the heterostructure systems, in which we have clearly demonstrated our ability to specify and distinguish between interface structures, we are able to apply the results of scattering theory to extract the key dynamical information concerning disordered systems. Through use of perturbation theory we can directly obtain the perturbed wave functions for large supercells (containing

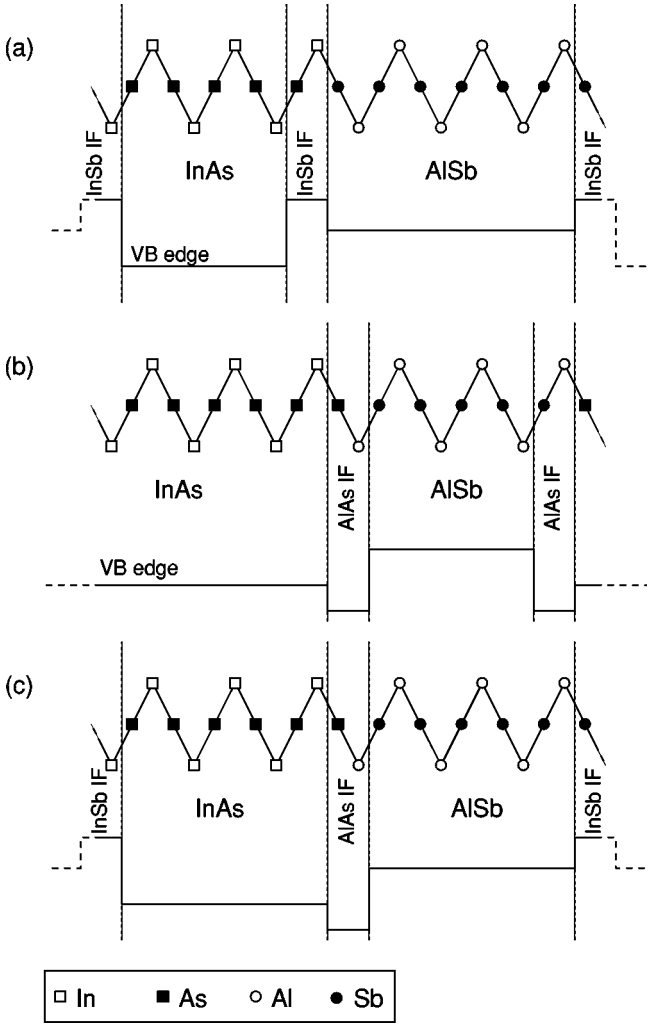

FIG. 1. Schematic diagrams of the three superlattice structures studied. Structure (a) has two InSb-like interfaces; (b) has two AlAs-like interface and structure; (c) has one of each interface type. Step potentials representing the valence band-edge lineups are presented, including the interface layers.

several million atoms), and following the method outlined in our previous publications,[18,19] we can relate the information contained in the perturbed wave functions to the scattering cross section through the *T* matrix. However, for the class of defects which we shall study in the present paper, namely isovalent substitutional anion and cation defects, we have shown that the *n*th-order result obtained by full application of the *T* matrix is almost identical to the simple first-order Born approximation (equivalent to Fermi's Golden Rule).[19] We therefore achieve considerable computational savings by the restriction to first order, evaluating the expression,

$$\sigma_n(\mathbf{k}) = \frac{2\pi}{\hbar}\frac{\Omega}{\mathbf{v}_0^{n\mathbf{k}}}\sum_{n'\mathbf{K}} |\langle \phi_{\mathbf{K}}^{n'}|U|\phi_{\mathbf{k}}^{n}\rangle|^2 \rho_{n'\mathbf{K}}(E_{n'K}), \qquad (1)$$

where $\sigma_n(\mathbf{k})$ is the scattering cross section from an initial state $\phi_{\mathbf{k}}^n$ in the unperturbed superlattice due to the perturbation Hamiltonian *U*. The summation $\Sigma_{n'\mathbf{K}}$ runs over all degenerate destination states, $\phi_{\mathbf{K}}^{n'}$, with partial density of states

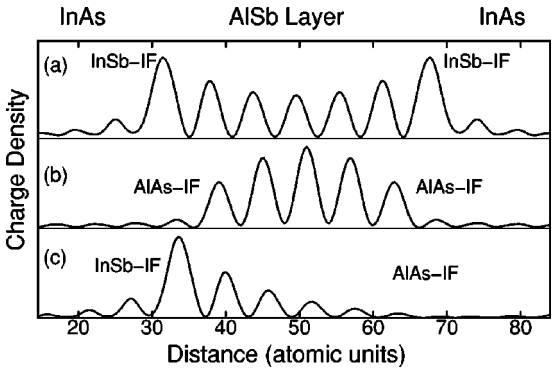

FIG. 2. The charge densities associated with the zone-center valence band-edge states are plotted for structures (a), (b), and (c). The charge densities were evaluated in the growth direction along the center of the atomic spiral. The different interface types are indicated, with the valence wells located in the center of the picture.

$\rho_{n'\mathbf{K}}(E_{n'K})$. The initial velocity of the carriers is $\mathbf{v}_0^{n\mathbf{k}}$ and Ω is the volume of the perturbed system unit cell.

III. ELECTRONIC BANDSTRUCTURES

The model of the AlSb/InAs heterostructures described above enables us to compare the electronic bandstructures associated with the different interface configurations. Since the expression for the cross section depends upon the density of destination states and initial electron velocities, it is clear that the electronic bandstructure will be critical to the final scattering cross sections. A study of the electronic bandstructures is therefore of more than just academic interest: it provides us with a link between the microscopic structural parameters and the scattering properties in which we are directly interested.

The structure (b), with two AlAs-like interfaces, has the most conventional band lineup (see Fig. 1), and presents a typical ground state valence band-edge charge density (see Fig. 2). We therefore expect that the band structure of this structure will be the most conventional in form. It is interesting to compare this with the band structures of (a) (two InSb-like interfaces) and (c) (one of each interface). Figure 3

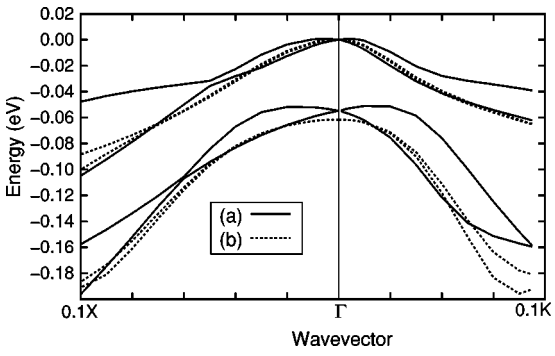

FIG. 3. The superlattice miniband energies (eV) are plotted for structure (a) (solid lines) and (b) (dashed lines) along key directions in the superlattice Brillouin zone. Γ is the zone center, *X* is the point on the zone boundary in the (100) direction, and *K* is the point on the zone boundary in the (110) direction.

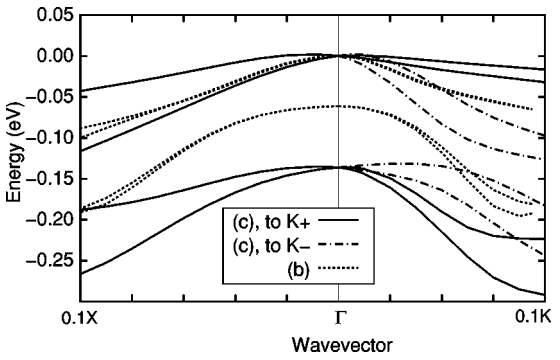

FIG. 4. The superlattice miniband energies (eV) are plotted for structure (c) (solid lines and dashed–dot lines) and (b) (dashed lines) along key directions in the superlattice Brillouin zone. Γ is the zone center, X is the point on the zone boundary in the (100) direction, $K+$ is the point on the zone boundary in the (110) direction, and $K-$ is the point on the zone boundary in the $(1\bar{1}0)$ direction. The reduced symmetry for structure (c) results in the difference between the $K+$ and $K-$ directions.

shows the detailed valence band structure (for the four uppermost valence minibands) for (b), and has superimposed the band structure of (a). While the zone center energy separations for these two structures are very similar, the miniband dispersions are rather different. Similarly, Fig. 4 compares the band structures of (b) and (c). The reduced symmetry of the structure (c), with different interface types, is clearly seen in the band structure by the inequivalence of the miniband dispersions along the $K+$ and $K-$ directions [defined as $(\frac{1}{2},\frac{1}{2},0)$ and $(\frac{1}{2},-\frac{1}{2},0)$, respectively]. It is clear then that the interface configuration is strongly reflected in the miniband structures of the superlattice structures, particularly for the near-band-edge valence states. The contrast between the three band structures close to the zone center is very clearly demonstrated by the plots of the valence band-edge energy surfaces in Fig. 5. The existence of interface localization in structures (a) and (c) dramatically alters the miniband dispersions. While structure (b), with no interface-localized states, has a typical superlattice band structure as expected, the InSb-like interfaces result in anomalous miniband curvatures.

Since the scattering cross sections depend upon the initial velocity of the electrons, and therefore upon the effective masses of the minibands, the radically different miniband dispersions for the three structures will be important in determining the strength of the scattering. Clearly, the nonparabolicity of these bands is very significant, and simple effective mass theory is not applicable. For the calculations of scattering cross sections which we present later, we use the *f*-sum rule to compute effective masses throughout the superlattice Brillouin zone. Since the scattering cross sections depend upon the initial velocity of the electrons, and therefore upon the effective masses of the minibands, the radically different miniband dispersions for the three structures will be reflected in the scattering cross sections.

As previously stated, the scattering is also dependent upon the density of scattering states available at any particular energy. It is clear by examination of the miniband dispersions of the three structures that their density of states will differ considerably. The detailed interface configuration of a structure determines the form of the density of states that enters the expression for the scattering cross section.

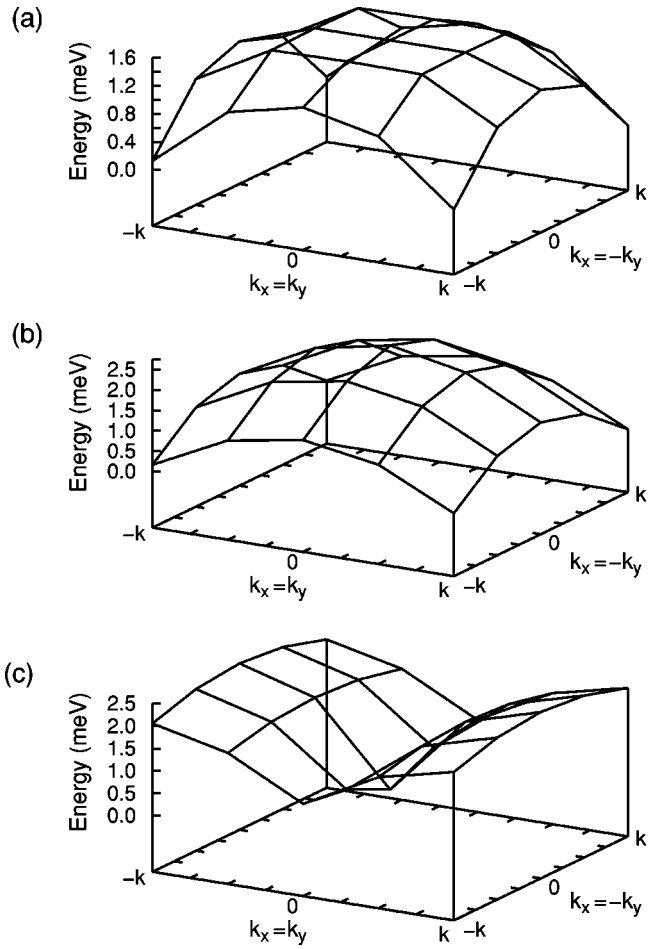

FIG. 5. The variation of the uppermost superlattice miniband in the region close to the zone center for the three structures (a), (b), and (c). The extent of the plot in the k_x and k_y directions is given by $k \approx 0.001(2\pi/a)$, where a is the in-plane lattice constant.

We have therefore identified a number of features in the superlattice band structures that are a specific result of the microscopic configuration of the atoms forming the heterointerfaces. These changes go beyond the simple energy shifts that we have previously reported,[12,13] and which can be understood qualitatively by a simple particle-in-a-box picture. However, such changes to the electronic band structure are, in themselves, of limited practical significance. Only when we can relate these changes to key device properties does their significance become apparent.

IV. SCATTERING CROSS SECTIONS OF SUBSTITUTIONAL DEFECTS

The valence band-edge wave functions, miniband dispersions, and densities of state were shown above to depend upon the microscopic interface structure. In this section, we examine the scattering cross sections related to simple substitutional defects for the three structures of different inter-

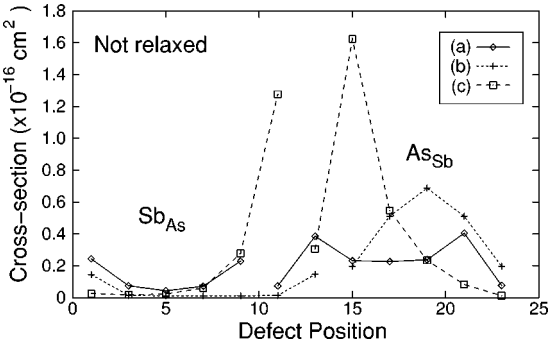

FIG. 6. The computed hole scattering cross section ($\times 10^{-16}$ cm^2) for isolated anion defects, plotted as a function of position in structures (a) (solid lines), (b) (short-dashed lines), and (c) (long-dashed lines). The positions are defined with respect to the beginning of the InAs layer, as shown in Fig. 1. No relaxation was included in the lattice surrounding the defects.

face configurations, and identify a signature of the interface localization. Since the interesting localizations occur in these structures for the valence band edges, we shall investigate the cross sections for holes close to the top of the valence band.

Let us first consider the case of isolated isovalent anion and cation defects in the structures, and initially make the assumption that there is no relaxation of the atoms surrounding the defects. Restricting our study to those defects that can arise from interdiffusion across the interface, we have computed the scattering cross sections of the anion defects Sb_{As} and As_{Sb} (where our notation Sb_{As} describes an antimony atom at the site of an As atom in the InAs layer), and the cation defects Al_{In} and In_{Al}. For each type of defect, we consider all of the possible sites within the superlattice unit cell and compare the cross sections for a particular wave vector in Figs. 6 and 7, respectively. If we examine first the variation of the anion cross sections, it is seen that the variation of cross section with position reflects the localization of charge in the valence band-edge states shown in Fig. 2. For structure (b), whose interface structure does not induce interface localization and which consequently exhibits a conventional ground state envelope function, we see that the maximum cross section occurs for defects located at the center of the valence well. In other words, the maximum cross section occurs when the defect is located at the center of the charge localization, maximizing the overlap integral. For structure (a), with two InSb-like interfaces localizing charge, the maximum cross section occurs for defect close to the interface, again corresponding to the peaks of the charge density. This trend is repeated for structure (c) where the strongly asymmetric wave function of the valence ground state is mirrored by the asymmetry in the position dependence of the anion defects. Examination of the cation defects, too, shows a ''wave function following'' in the magnitude of the scattering cross sections.

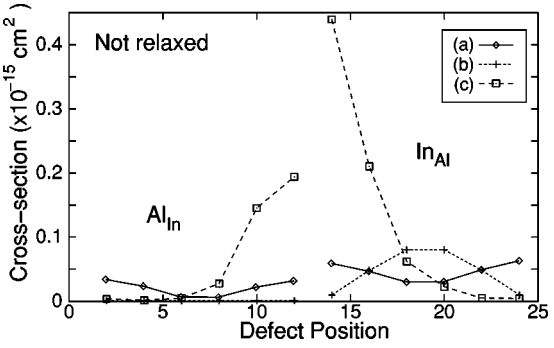

FIG. 7. The computed hole scattering cross section ($\times 10^{-15}$ cm^2) for isolated cation defects, plotted as a function of position in structures (a) (solid lines), (b) (short-dashed lines), and (c) (long-dashed lines). The positions are defined with respect to the beginning of the InAs layer as shown in Fig. 1. No relaxation was included in the lattice surrounding the defects.

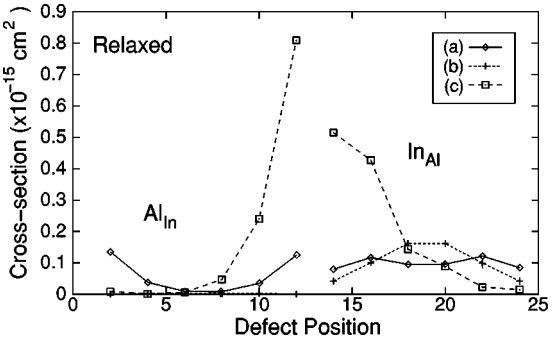

FIG. 8. The computed hole scattering cross section ($\times 10^{-15}$ cm^2) for isolated cation defects, plotted as a function of position in structures (a) (solid lines), (b) (short-dashed lines), and (c) (long-dashed lines). The positions are defined with respect to the beginning of the InAs layer, as shown in Fig. 1. Full relaxation was included in the lattice surrounding the defects.

Given the nature of the expression for the cross section, and considering the probability of the system ''sampling'' the defects, it is not surprising that this mirroring of the wave functions occurs. However, it is important in the context of the practical significance of the cross sections—the scattering cross sections provide us with a means of probing the wave function localizations. In our previous studies of localization in InAs/AlSb structures, we have only been able to identify rigid energy shifts as an observable signature of the interface-induced localizations. The above calculations indicate that it may be possible to obtain an unambiguous signature of the interface effects through the scattering cross sections.

In a number of previous papers we have shown that the role of lattice relaxation may be significant in determining the scattering properties of hole cross sections for anion defects.[18,19] It is important to assess the role of relaxation in the AlSb/InAs structures, as this might qualitatively change the distributions obtained above. In Fig. 8 we present the results of calculations for the cation defects with full relaxation of the surrounding atoms included through a valence force field model. Direct comparison with Fig. 7 reveals that the cation position dependence remains largely unaffected by the inclusion of lattice relaxation.

In contrast, the variations of the anion cross sections with position are seen to change significantly upon the relaxation of the atoms surrounding the defects. Figure 9 compares the

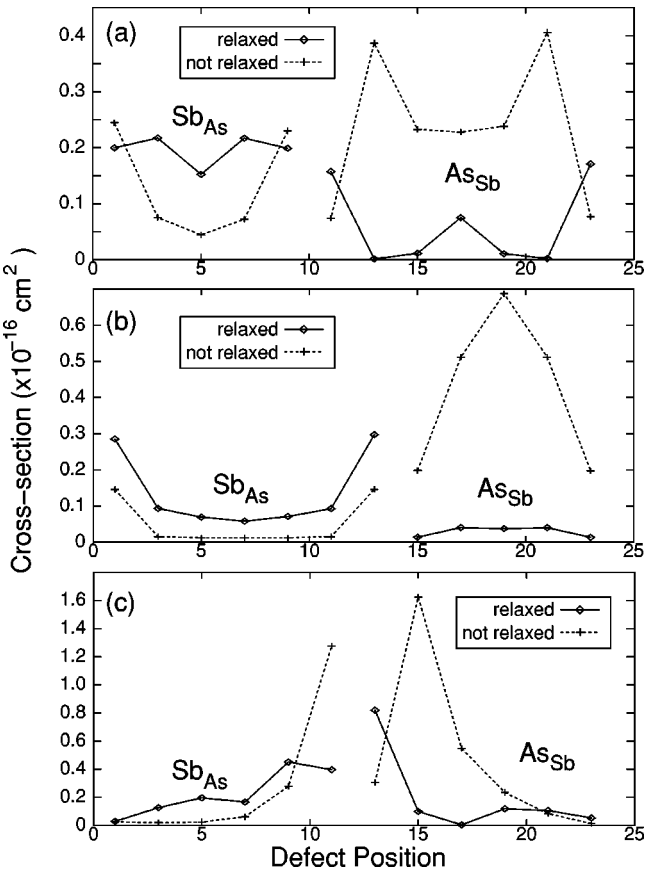

FIG. 9. The computed hole scattering cross section ($\times 10^{-16}$ cm^2) for isolated cation defects, plotted as a function of position in structures (a), (b), and (c). The positions are defined with respect to the beginning of the InAs layer, as shown in Fig. 1. For each structure, the cross section computed, including full relaxation of the lattice surrounding the defects (solid lines), is compared to the calculation with no relaxation (dashed lines).

relaxed and unrelaxed cross sections for each structure. In each case the dependence of the cross section upon defect position changes considerably as the relaxation of the lattice is included. In particular, the effect of lattice relaxation is to break down the direct link between the wave function envelope and the cross-section maximum. The general mechanism by which this may happen is not difficult to identify. Since the perturbation to the system induced by the defect now includes also the effect of a large number of atoms in the lattice moving, the spatial extent of the perturbation becomes larger and incorporates many more individual and competing contributions. However, we have not yet been able to answer the question as to why the anion and cation defects should behave so differently in this respect, or to identify the particular microscopic mechanisms providing for the cancellations of anion scattering strength. These features of the role of lattice relaxation in determining the scattering properties remain the subject of our on-going research.

Although it is not as simple to relate the dependence of the anion cross section to the localization of the valence band-edge wave functions, the position dependence of the anion cross section remains easily distinguishable between the different interface configurations. While the cation position dependence was, in essence, qualitatively predictable from a simple particle-in-a-box model, the signature of the anion position dependence requires a full microscopic model of the system.

V. CONCLUSION

The strain-dependent empirical pseudopotential calculations of AlSb/InAs superlattices reproduce the interface localizations predicted from earlier studies, and as proposed by Kroemer *et al.*[16] Comparison of a systematic series of structures has demonstrated that the superlattice band structures and wave functions reflect the microscopic interface configurations present. However, previous treatment of these structures has been able to make predictions only of simple energy shifts associated with the interface potentials. Although these energy shifts are in agreement with experimental observation, they are not sufficient to provide an unambiguous signature of the wave function localizations discussed.

The scattering cross-section calculations that we have presented have enabled us to probe the valence band-edge wave functions, and extract a microscopic signature of the interface localizations that could, in principle, be verified experimentally. We have predicted a behavior for which a direct link to the microscopic charge localizations exists. The unambiguous identification of the localizations related to the interface configurations, and the understanding of the role of defect distribution on scattering properties of these structures, represent important practical issues for the future application of these structures in AlSb/InAs devices.

Since the theoretical tools that we have applied are generic methods and applicable to a wide variety of material systems, the process of probing for localization at interfaces through the study of scattering properties, as developed in this paper, should itself be applicable to the investigation of interface localization across a broad range of heterostructure systems.

ACKNOWLEDGMENTS

We would like to thank the U.S. Office of Naval Research, U.K. Engineering and Physical Science Research Council, and D. E. R. A. (Malvern, U.K.) for financial support.

*Author to whom correspondence should be addressed; FAX: +44 191 222 7361; Electronic address: milan.jaros@ncl.ac.uk

[1] X. C. Cheng and T. C. McGill, J. Cryst. Growth **208**, 183 (2000).
[2] X. C. Cheng and T. C. McGill, J. Appl. Phys. **86**, 4576 (1999).
[3] J. Smoliner, R. Heer, and G. Strasser, Phys. Rev. B **60**, R5137 (1999).
[4] S. Gardelis, C. G. Smith, C. H. W. Barnes, E. H . Linfield, and D. A. Ritchie, Phys. Rev. B **60**, 7764 (1999).
[5] K. Ohtani and H. Ohno, Electron. Lett. **35**, 935 (1999).
[6] J. B. Boos, B. R. Bennett, W. Kruppa, D. Park, J. Mittereder, R. Bass, and M. E. Twigg, J. Vac. Sci. Technol. B **17**, 1022 (1999).
[7] C. R. Bolognesi, M. W. Dvorak, and D. H. Chow, IEEE Trans.

Electron Devices **46**, 826 (1999).
[8] K. Nomoto, K. Taira, T. Suzuki, and I. Hase, J. Appl. Phys. **85**, 953 (1999).
[9] J. B. Boos, M. J. Yang, B. R. Bennett, D. Park, W. Kruppa, C. H. Yang, and R. Bass, Electron. Lett. **34**, 1525 (1998).
[10] B. Brar, J. Ibbetson, H. Kroemer, and J. H. English, Appl. Phys. Lett. **64**, 3392 (1994).
[11] G. Tuttle, H. Kroemer, and J. H. English, J. Appl. Phys. **67**, 3032 (1990).
[12] M. J. Shaw, P. R. Briddon, and M. Jaros, Phys. Rev. B **52**, 16 341 (1995).
[13] M. J. Shaw, G. Gopir, P. R. Briddon, and M. Jaros, J. Vac. Sci. Technol. B **16**, 1794 (1998).
[14] D. J. Chadi, Phys. Rev. B **47**, 13 478 (1993).
[15] J. Shen, H. Goronkin, J. D. Dow, and S. Y. Ren, J. Appl. Phys. **77**, 1576 (1995).
[16] H. Kroemer, C. Nguyen, and B. Brar, J. Vac. Sci. Technol. B **10**, 1769 (1992).
[17] J. Spitzer, A. Höpner, M. Kuball, M. Cardona, B. Jenichen, H. Neuroth, B. Brar, and H. Kroemer, J. Appl. Phys. **77**, 811 (1995).
[18] M. J. Shaw, Phys. Rev. B **61**, 5431 (2000).
[19] M. J. Shaw, E. A. Corbin, M. R. Kitchin, J. P. Hagon, and M. Jaros, J. Vac. Sci. Technol. B **18**, 2088 (2000).